

# Ring-like defect formation in n-type Czochralski-grown silicon wafers during thermal donor formation

*Rabin Basnet\*, Hang Sio, Manjula Siriwardhana, Fiacre E. Rougieux, Daniel Macdonald*

R. Basnet, Dr. H. Sio, M. Siriwardhana, Prof. D. Macdonald

Research School of Electrical, Energy and Materials Engineering, The Australian National University, Canberra, ACT 2601, Australia

E-mail: [rabin.basnet@anu.edu.au](mailto:rabin.basnet@anu.edu.au)

Dr. F. E. Rougieux

School of Photovoltaic and Renewable Energy Engineering, The University of New South Wales, Sydney, New South Wales, Australia

**Keywords:** Czochralski-grown silicon, thermal donors, ring defects, oxygen precipitation, thermal history

This paper presents experimental and simulation studies on the formation of recombination-active ring-like defects during thermal donor formation at 450 °C in *n*-type Czochralski-grown silicon wafers. With increasing anneal duration from 1 hr to 24 hrs, the resistivity and interstitial oxygen concentration of samples decrease, consistent with the formation of thermal donors. However, after a subsequent thermal donor annihilation treatment, the resistivity recovers completely, while the interstitial oxygen concentration recovers only partially. Furthermore, the wafers exhibit ring-like defects in photoluminescence images after the thermal donor generation and remain persistent even after annihilation treatment. By applying a *tabula rasa* treatment prior to thermal donor generation anneals, the net loss of interstitial oxygen is reduced, and the incubation time of the ring-like defects is extended in comparison to as-grown wafers. Finally, to investigate the possibility of low-temperature

This article has been accepted for publication and undergone full peer review but has not been through the copyediting, typesetting, pagination and proofreading process, which may lead to differences between this version and the [Version of Record](#). Please cite this article as doi: [10.1002/pssa.202000587](https://doi.org/10.1002/pssa.202000587)

This article is protected by copyright. All rights reserved

precipitation, simulation of oxygen precipitation kinetics during the 450 °C annealing steps is performed using an enhanced effective diffusivity of oxygen. These simulations demonstrate that oxygen precipitation can occur simultaneously during thermal donor formation, resulting in recombination-active ring-like defects.

## 1.0 Introduction

Czochralski-grown silicon (Cz-Si) wafers are now the dominant material for silicon solar cell productions. A substantial fraction (up to 15%) of a Cz-Si ingot contains carrier-lifetime limiting defects in the as-grown state, and subsequent processing of solar cells can create further bulk defects [1], [2]. These defects often manifest as circular features such as discs [1] or rings [1]–[4] in various imaging techniques. Many ring-like defects are the result of the formation of oxygen-related defects, namely thermal donors (TD) [5], [6], oxygen precipitates (OP) [7], [8], and oxidation-induced stacking faults (OISF) [9]. TDs are formed when a Cz-Si wafer is subjected to a low-temperature (300 °C – 500 °C) anneal [10]–[12]. Fortunately, TDs are annihilated by annealing above 650 °C for a short duration ( $\leq 30$  min), followed by relatively fast cooling [13],[14]. Therefore, ring-like features induced by TDs usually disappear in the fabrication of homo-junction solar cells as they are dissociated during high-temperature processes, such as dopant diffusions. OISF nuclei are formed during ingot cooling and are activated only after a high-temperature ( $> 1000$  °C) oxidation [15]. On the other hand, ring defects induced by OPs usually appear only after subjecting wafers from intermediate to high-temperature (650 °C – 1100 °C) heat treatments. The onset of ring defects in this temperature range depends on the wafer properties (thermal history, initial interstitial oxygen concentration  $[O_i]$ , carbon concentration) and process parameters such as temperature, duration, and ambient, which all determine the oxygen precipitation behavior [7], [8], [16]. These OP-related ring defects persist even after cell fabrication is complete, and can significantly reduce solar cell performance [1], [17].

However, the potential formation of persistent ring-like defects at lower temperatures (300 °C – 500 °C), which is the temperature range over which thermal donors are formed, has not been fully investigated. At these temperatures, the diffusivity ( $D_o$ ) of interstitial oxygen ( $O_i$ ) extrapolated from higher temperatures is very low [18]. For example, the diffusion lengths of  $O_i$  for 1 hour at 450 °C and 900 °C are estimated to be 0.1  $\mu\text{m}$  and 0.8  $\mu\text{m}$ , respectively. As a result, OP growth kinetics are expected to be largely limited by  $O_i$  diffusion at low temperatures. However, evidence of the formation of OPs at lower temperatures is reported in Refs [19], [20] based on the appearance of broad infrared absorption peaks at 1060  $\text{cm}^{-1}$  and rod-like defects in transmission electron microscopy. In a typical Cz-Si ingot, some of the seed-end wafers contain ring-like defects in the as-grown state which do not disappear even after TD annihilation treatment. As a result, a certain portion of seed-end wafers is not used for solar cell fabrication, increasing the material wastage and operational cost. In conventional Cz-Si ingot growth, the seed-end of the ingot has the longest dwell time at the 300 °C – 500 °C temperature interval. This extended low-temperature could contribute to the formation of ring-like defects other than TD.

In this study, we investigate ring-like defects formed intentionally *via* low-temperature annealing in commercially available Cz-Si wafers. We corroborate our experimental findings with the support of simulations. Further, we perform a high-temperature pre-annealing step, known as *tabula rasa* for the negation of the thermal history [3], [16], [21], and analyze its impact on subsequent defect formation kinetics. This study aims to elucidate the potential impact of an extended ingot dwelling time at relatively low-temperatures on the formation of ring-like defects and provide evidence to design the well-controlled growth conditions of Cz-Si ingot to suppress recombination-active defect generation.

## 2.0 Experimental details

The samples used in this work were commercially available  $10\ \Omega\cdot\text{cm}$   $n$ -type Cz-Si wafers. 4-inch wafers were cleaved into four quarters. All samples were then saw-damage-etched in tetramethylammonium hydroxide solution to remove  $10 - 12\ \mu\text{m}$  from each side, with a final thickness of  $290\ \mu\text{m}$ . Samples were cleaned using an RCA cleaning process prior to each high-temperature step. To assess the impact of a pre-annealing step, some of the samples were subjected to a *tabula rasa* (TR) step in a quartz tube furnace. The TR step was performed at  $1100\ ^\circ\text{C}$  for 30 min in oxygen with loading and unloading at  $700\ ^\circ\text{C}$  and ramp-up rate of  $15\ ^\circ\text{C}/\text{min}$  and cooling rate of  $30\ ^\circ\text{C}/\text{min}$ . The TR temperature and duration in this work was selected based on our previous work on the TR conditions optimization for the mitigation of ring defects in  $n$ -type Cz-Si wafers [16]. Such samples are referred to as the TR-treated samples. Then, the TR-treated and as-grown samples were subjected to TD generation anneals in a quartz tube furnace. We selected the most commonly studied temperature of  $450\ ^\circ\text{C}$  and annealed for 1 hr, 2 hrs, 4 hrs, and 24 hrs in nitrogen. The samples were loaded and unloaded at  $450\ ^\circ\text{C}$  and maintained a nitrogen flow rate of 20 L/hr during annealing. We note that the long anneal duration of 24 hrs is not a typical dwell time for a Cz ingot between  $500\ ^\circ\text{C} - 350\ ^\circ\text{C}$ . Such a condition is chosen in this work to ensure a high TD concentration. Further, the generated TDs were annihilated by subjecting the samples to a  $650\ ^\circ\text{C}$  anneal for 30 min in nitrogen in a quartz tube furnace, which we refer to as a TD annihilation treatment. During the TD annihilation step, samples were loaded and unloaded at  $650\ ^\circ\text{C}$  and maintained a nitrogen flow rate of 20 L/hr during annealing. For this duration, the so-called “new donors” are not expected to form [22], and therefore we ignore any impact of the new donors.

For carrier lifetime measurements and photoluminescence (PL) images samples were passivated using plasma-enhanced chemical vapor deposited (PECVD) (Roth and Rau

AK400) silicon nitride films, deposited at a substrate temperature of 300 °C for 3 min. This relatively low thermal budget is assumed to have no impact on the formation and dissolution of TDs and OPs. Carrier lifetimes were measured using the quasi-steady state photoconductance and transient photoconductance decay techniques with a WCT-120 tool from Sinton Instruments [23]. The resistivity of the samples after each heat treatment step was extracted during the lifetime measurement. The resistivity obtained from WCT-120 tool is expressed as the dark conductance which is calibrated to four-point measurements. PL images were captured using an LIS-R1 PL imaging tool from BT imaging [24].

All the thermal oxide layers formed during annealing steps and dielectric passivation were removed by hydrofluoric acid before Fourier-transform infrared spectroscopy (FTIR) measurements. The  $[O_i]$  concentration was measured by FTIR, using a Bruker Vertex 80 tool and calibrated using the ASTM F121-83 standard with a calibration coefficient of  $2.45 \times 10^{17} \text{ cm}^{-2}$  at room temperature. The as-grown sample had an  $[O_i]$  of  $8.5 \times 10^{17} \text{ cm}^{-3}$ . Carbon concentrations in the samples were below the detection limit ( $1.0 \times 10^{16} \text{ cm}^{-3}$ ) of FTIR at room temperature.

### 3.0 Results

#### 3.1 Evolution of resistivity and TD concentration

The resistivities of the sample decreased with an increasing TD generation anneal duration, as shown in **Figure 1**. TDs are known to occur in a double-ionized state at room temperature [25], [26], and the resulting extra free electron concentration is therefore, twice the [TD], resulting in a corresponding decrease in the resistivity of our *n*-type wafers. [TD] can be determined using the change in resistivity ( $\rho$ ) as follows.

$$\rho = \frac{1}{q \times \mu_{elec} \times ([P] + 2 \times ([TD]_{ini} + [TD]_{anneal}))} \quad (1)$$

Where  $q$  is the elementary charge,  $\mu_{elec}$  is the electron mobility,  $[P]$  is the phosphorus dopant concentration,  $[TD]_{ini}$  is the initial grown-in TD concentration, and  $[TD]_{anneal}$  is the concentration of TDs formed during the TD generation anneal.

TD formation at a given temperature is known to depend on both the  $[O_i]$  and anneal duration [27], [28]. The evolution of the TD concentration  $[TD]$  at 450 °C can be empirically described by Wijaranakula's model [28], which predicts a linear increase of  $[TD]$  with the TD generation anneal duration until a maximum concentration is reached, after which it decreases again, as shown in **Figure 1**. We observe a slightly higher measured  $[TD]$  in our samples than the  $[TD]$  predicted by Wijaranakula's model. This is due to the thermal history of the sample discussed further in Section 3.4.

After the TD generation treatment, the wafers were subjected to the TD annihilation step. We observed a complete recovery of the resistivity in all the samples, which infers a successful annihilation of electrically-active TDs, as shown in **Figure 1**. Note the resistivity of the as-grown sample was 10  $\Omega \cdot \text{cm}$ , which increased slightly to 11  $\Omega \cdot \text{cm}$  after TD annihilation, so we estimated the grown-in  $[TD]$  to be  $2.5 \times 10^{13} \text{ cm}^{-3}$ .

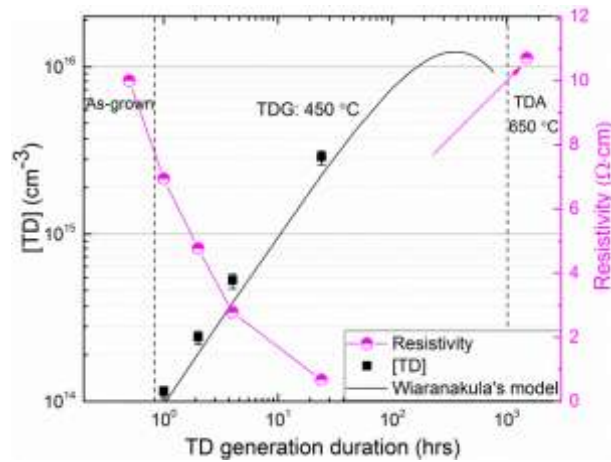


**Figure 1:** Evolution of resistivity and  $[TD]$  computed from the resistivity as a function of TD generation anneals duration for the as-grown samples. The line shows the TD concentrations predicted by Wijaranakula's model [28]. Note we assume all TDs are annihilated after TD annihilation step.

### 3.2 Loss of $[O_i]$

**Figure 2** shows the evolution of  $[O_i]$  in the as-grown samples after subjecting them to the TD generation treatment (450 °C in nitrogen) for 1 hr, 2 hrs, 4 hrs, and 24 hrs and followed by the subsequent TD annihilation (650 °C for 30 min) step. As expected, we observe a loss in  $[O_i]$  with increasing TD generation duration, due to the sequential clustering of  $O_i$  to form different species of TDs [10]–[12]. In the subsequent TD annihilation step, the TDs are annihilated, as evidenced by the complete recovery of the resistivity in **Figure 1**. However, we do not observe a corresponding complete recovery of  $[O_i]$ , as shown in **Figure 2**. The net loss of  $[O_i]$  increases with the TD generation duration. This incomplete recovery of  $[O_i]$  indicates the possible formation of other oxygen-related defects simultaneously with TDs during the 450 °C anneal.

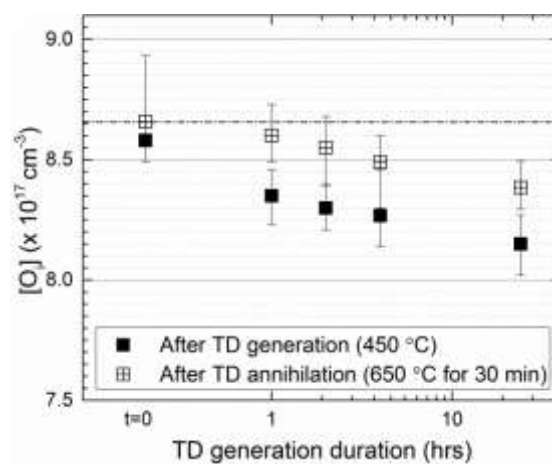


**Figure 2:** FTIR measured  $[O_i]$  in the as-grown samples after subjecting them to different durations of the TD generation anneal and followed by a subsequent TD annihilation step.

### 3.3 PL images

**Figure 3** presents PL images of the surface-passivated samples after the TD generation anneals of 4 hrs and 24 hrs, followed by TD annihilation. TD generation durations of less than 4 hrs did not induce any recombination-active defects in the PL images. However, for TD generation of 24 hrs, we observed distinct ring-like defects. More importantly, such ring-like structures do not disappear even after TD annihilation. This strongly suggests that such ring-like defects are not due to TDs but possibly from other defects. Note that the samples used in this work are commercially available wafers. In reality, the incubation time for ring-like defects may be significantly shorter for samples from the seed-end of Cz-Si ingot.

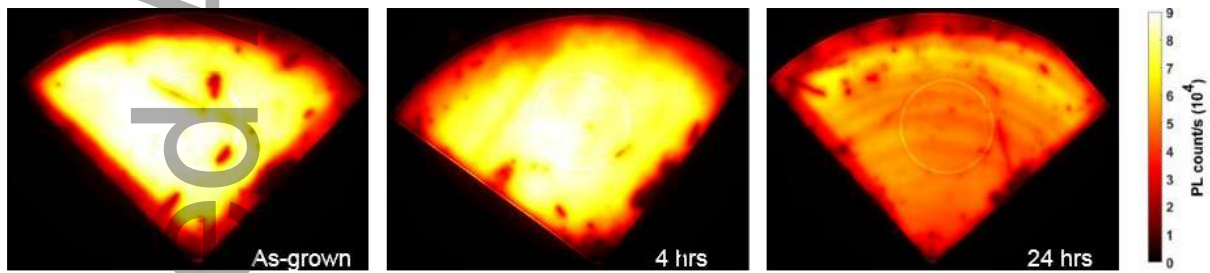


**Figure 3:** PL images before and after TD generation of 4 hrs and 24 hrs and followed by the TD annihilation step. All of the images were captured at a constant illumination intensity of 1 sun and an exposure time of 0.7 seconds. Note the dark edge in the samples is due to the edge-effect of PECVD deposited silicon nitride.

### 3.4 Impact of *tabula rasa*

**Figure 4** shows the evolution of [TD] and [O<sub>i</sub>] in the TR-treated samples after subjecting them to a TD generation treatment (450 °C in nitrogen) for 1 hr, 2 hrs, 4 hrs, and 24 hrs and followed by the subsequent TD annihilation (650 °C for 30 min) step. In comparison to the as-grown samples, the TR-treated samples have a smaller [TD] and show a much better agreement with the theoretical [TD] predicted by Wiaranakula's model. This is likely due to



the dissolution of grown-in TD nuclei during the TR step, ensuring that  $[TD]_{ini} = 0$ . During the initial stage of TD generation, the formation of TDs is dominated by grown-in TD nuclei [29]. However, after sufficiently long TD generation durations, TDs formed *via* new TD nuclei formed during annealing are expected to dominate [30]. Furthermore, similar to the as-grown samples, the TR-treated samples also showed an incomplete recovery of  $[O_i]$  after TD annihilation. This further adds evidence that the loss in  $[O_i]$  is not only due to the possible growth of grown-in OP nuclei but also to the formation of oxygen-related defects during the course of the TD generation treatment.

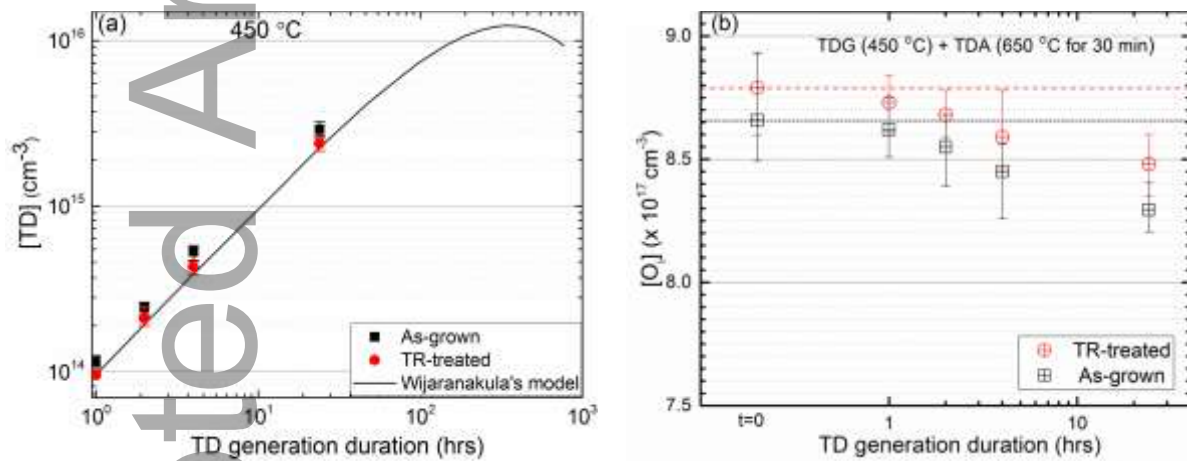


**Figure 4:** (a) Evolution of  $[TD]$  calculated from the change in resistivity in the TR-treated and as-grown samples after subjecting to different duration of TD generation anneals. (b) Evolution of  $[O_i]$  measured with FTIR in the TR-treated samples in comparison to the as-grown samples after subjecting to different duration TD generation anneals followed by TD annihilation. The line in (a) shows the TD concentrations predicted by Wijaranakula's model [28].

**Figure 5** presents the PL images of the TR-treated samples after the TD generation anneals followed by TD annihilation. Unlike the as-grown samples, the TR-treated samples do not show any obvious recombination-active ring-like defects after 24 hrs of TD generation treatment. However, further anneal (48 hrs) lead to the formation of ring-like defects. We

have previously observed a similar delay in the onset of ring defects in TR-treated samples in comparison to as-grown samples subjected to high-temperature anneals [16]. We proposed that was due to the dissolution of grown-in OPs by TR, resulting in slower oxygen precipitation kinetics during subsequent heat treatments. A similar delay phenomenon in this work brings further evidence to the suggestion that these ring-like defects are also related to OPs.

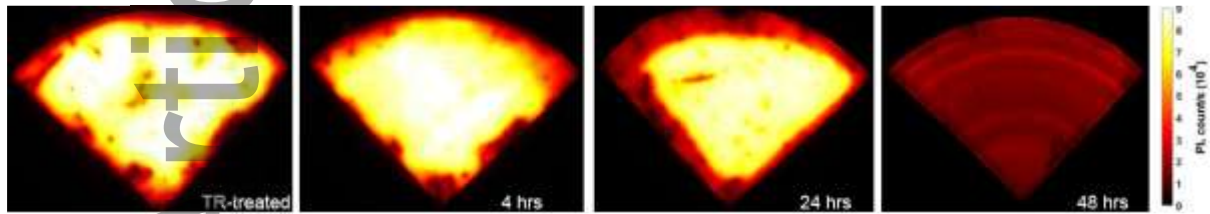


**Figure 5:** PL images of the TR-treated samples before and after TD generation of 4 hrs, 24 hrs, and 48 hrs and followed by the TD annihilation step. All of the images were captured at a constant illumination intensity of 0.7 suns and an exposure time of 1 second. Note the dark edges in the samples is due to the edge-effect of PECVD deposited  $\text{SiN}_x\text{:H}$ .

#### 4.0 Discussion of results

Previously, several studies have attributed ring defects observed in the PL images of Cz-Si wafers to recombination-active OP [7], [8], [31]. However, such samples were typically subjected to intermediate to high-temperature (650 °C – 1100 °C) heat treatments, which favored both the nucleation and growth of OPs [32]. In principle, ring-like defects formed during low temperature anneals may be related to vacancy-related defects, TD, OP, or impurities, which could all play a role in the formation of rings either in isolation or in combination. In this work, persistent ring-like defects are generated at 450 °C, ruling out the involvement of some of the recombination-active vacancy-related grown-in defects such as vacancy-phosphorus (V-P) pairs and vacancy-oxygen (V-O) pairs. Previous work has shown

that V-P and V-O pairs are dissociated at 170 °C and 350 °C, respectively [28],[29]. Similarly, lifetime-limiting defects remain after TD annihilation treatment, thus such defects are not related to electrical-active TD. Therefore, the combined evidence of distinct ring-like defects and a net loss of  $[O_i]$  suggest that the ring-like defects are related to oxygen precipitation.

Oxygen precipitation kinetics depends on the complex interplay of thermal budget, interstitial oxygen concentration, and point defect concentrations [32]–[34]. The relatively high initial  $[O_i]$  ( $8.5 \times 10^{17} \text{ cm}^{-3}$ ) present in the samples used in this work favors oxygen precipitation. However, the diffusivity of  $O_i$  ( $D_o$ ) at 450 °C obtained from the extrapolated equation,  $D_o = 0.13 \exp(-2.53/kT) \text{ cm}^2\text{s}^{-1}$  [18] is  $3 \times 10^{-19} \text{ cm}^2\text{s}^{-1}$ . This is too low to promote any substantial oxygen precipitation at 450 °C. Nevertheless, at low-temperatures ( $< 700 \text{ °C}$ ), the presence of oxygen dimers ( $O_{2i}$ ) affects the effective diffusivity of oxygen. Åberg *et al.* [35] demonstrated that oxygen dimers diffuse faster ( $\sim 10^6$  times) than  $O_i$  at 400 °C [35]. Further, Kissinger *et al.* [36] demonstrated that oxygen dimers are present in smaller concentrations ( $< 10^{15} \text{ cm}^{-3}$ ) than the total oxygen concentration [36]. However, they become important in regard to the transport capacity of oxygen at low-temperatures and accelerate the formation kinetics of thermal donors. Therefore, fast diffusing oxygen dimers contribute to the enhancement of the effective diffusivity of oxygen at low-temperatures. Previous studies [37], [38] corroborate an enhanced diffusivity of oxygen during the low-temperature heat-treatments. Further, Takeno *et al.* [39] have calculated the effective oxygen diffusivities in the range of  $2 - 4 \times 10^{-14} \text{ cm}^2\text{s}^{-1}$  between 400 °C – 700 °C based on the extended nucleation theory [40]. Based on the enhanced oxygen diffusivities, Kelton [41] has demonstrated enhanced OP nucleation, and Takeno *et al.* [39] have presented enhanced growth rates of OPs below 700 °C. Therefore, we have considered the effective diffusivity of oxygen to be  $3 \times 10^{14} \text{ cm}^2\text{s}^{-1}$  at 450 °C. Using such an enhanced diffusivity, we then simulate oxygen

precipitation at low temperatures by solving a set of kinetic rate equations for each possible precipitate as implemented in Refs. [42], [43].

## 5.0 Simulation of oxygen precipitation

The simulations of oxygen precipitation in this work are based on the freely available implementation developed by B. C. Trznadlowski [42], [43]. The detailed description of the model can be found in the Refs. [42], [43]. A brief introduction of the model is discussed below. The evolution of  $[O_i]$  and the size of OPs can be expressed as kinetic rate equations [42], [43]:

$$\frac{\partial C_o}{\partial t} = D_o \nabla^2 C_o - \sum_2^\infty n \frac{\partial f_n}{\partial t} \quad (2)$$

$$\frac{\partial f_n}{\partial t} = R_n - R_{n+1}, n = 2 \dots \infty \quad (3)$$

where  $C_o$  is the oxygen concentration,  $D_o$  is the diffusivity of interstitial oxygen,  $f_n$  is the concentration of oxygen precipitates containing  $n$  oxygen atoms, and  $R_n$  is the net rate of growth from size  $n-1$  to  $n$ , which can be expressed as [42], [43]:

$$R_n = g_{n-1} f_{n-1} - d_n f_n \quad (4)$$

where  $g_n$  is the rate of growth from size  $n$  to  $n+1$  and  $d_n$  is the rate of dissolution from size  $n$  to  $n-1$ . The definitions of growth and dissolution rate can be found in the refs [42], [43]. In reality, precipitates adjust their morphology in order to minimize free energy and are influenced by point defects. However, in this work, oxygen precipitates are modeled as spheres with radius ( $r_n$ ) [42], [43].

$$r_n = \left( 3 n \frac{V_{SiO_2/2}}{4\pi} \right)^{1/3} \quad (5)$$

where  $V_{SiO_2}$  is the molecular volume of  $SiO_2$ , which is assumed to be  $4.35 \times 10^{-23} \text{ cm}^3$ .

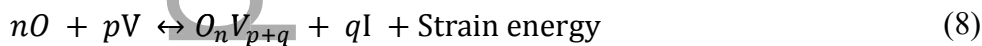
The growth and dissolution rate are considered as diffusion-limited processes and can be expressed as follows [42]–[44]:

$$g_n = \frac{4\pi^* r_n^2}{a + r_n} D_o C_o \quad (6)$$

$$d_n = g_{n-1} \exp(\Delta G_n/kT) \quad (7)$$

Where  $a$  is on the order of the silicon lattice constant ( $5.43 \times 10^{-8}$  cm),  $k$  is Boltzmann's constant,  $T$  is temperature, and  $\Delta G_n$  is the total change in free energy upon forming a size  $n$  precipitate.

The newly formed OP *via* aggregation of several atoms causes a volume mismatch in the silicon lattice and results in a compressively strained OP [45]. For the continuation of oxygen precipitation, there must be a mechanism to release this compressive strain. In defect-free silicon, homogenous nucleation can occur by relieving the strain *via* intrinsic point defects, either by the ejection of self-interstitials (I) from the precipitate/matrix interface or by absorption of silicon lattice vacancies (V) by the precipitates [45] as follows.



Where  $O_n V_{p+q}$  refers to an OP containing  $n$  oxygen atoms that has consumed  $p$  silicon vacancies and ejected  $q$  interstitials.

Note that oxygen and nitrogen ambient can lead to the injection of interstitials or vacancies from the surface during thermal treatment. Such intrinsic point defects subsequently diffuse in the wafer and can affect the precipitation kinetics. In our simulation, such point defect injection from the surface is not taken into account as the diffusivity of intrinsic point defects is insignificant at the simulated temperatures.

## 5.1 Application of the model in this work

The model developed by Trzynadlowski [42], [43] is primarily validated for the temperature range of 750 °C – 1050 °C. However, for heat-treatments at 450 °C, the model requires tuning of temperature-dependent parameters, particularly the diffusivity and the solubility of oxygen. As mentioned in Section 4.0, we assume an enhanced diffusivity of oxygen ( $3 \times 10^{-14} \text{ cm}^2\text{s}^{-1}$ ) for temperatures below 600 °C. Since the ingot growth conditions are not known accurately, we are not able to estimate the initial distribution of OPs or the net concentrations of intrinsic point defects. The size and density distribution of grown-in OPs cannot be obtained by any traditional method such as laser scattering tomography (LST). Therefore, we assume a range of initial net point defect concentrations and dwell times for the ingot at 600 °C and 450 °C.

## 5.2 Simulation of grown-in conditions

The grown-in [TD] for the samples used in this work is estimated as  $2.5 \times 10^{13} \text{ cm}^{-3}$ , as explained above. We therefore approximate the 450 °C dwell time during ingot cooling to be 1 hr. Further, based on the grown-in [TD], we could assume that the samples used in this work originate from a solidification fraction of 50% – 65% with a resulting dwell time between 600 °C – 900 °C representing OP nucleation and growth during ingot cooling of 10 hr [46]–[48].

To test the influence of the initial point defect concentrations, we simulate the evolution of the grown-in spectral size distribution of OPs with a range of vacancy-rich conditions likely to occur in commercial Cz silicon for PV applications. The initial  $[\text{O}_i]$  measured by FTIR ( $8.5 \times 10^{17} \text{ cm}^{-3}$ ) and assumed thermal history (600 °C for 10 hrs + 450 °C for 1 hr) are used to simulate the evolution of the grown-in spectral size distribution of OPs, as shown in **Figure 6 (a)**. For the chosen net vacancy concentrations, the average size of OPs remains similar and as expected, with the spectral distribution increasing with the net vacancy concentration.

We then keep the vacancy concentration constant at  $4 \times 10^{12} \text{ cm}^{-3}$ , and examine the impact of a range of dwell times at 600 °C (2, 4, 8, 10, 12, 16, and 20 hrs), as shown in **Figure 6 (b)**. For the given conditions, the average size of OPs remained similar to the increase in the dwell duration. Therefore, from these initial condition results, we have selected an initial condition of net vacancy concentration of  $4 \times 10^{12} \text{ cm}^{-3}$  and thermal history of 600 °C for 10 hrs + 450 °C for 1 hr for the further simulations of heat-treatments performed in this work.

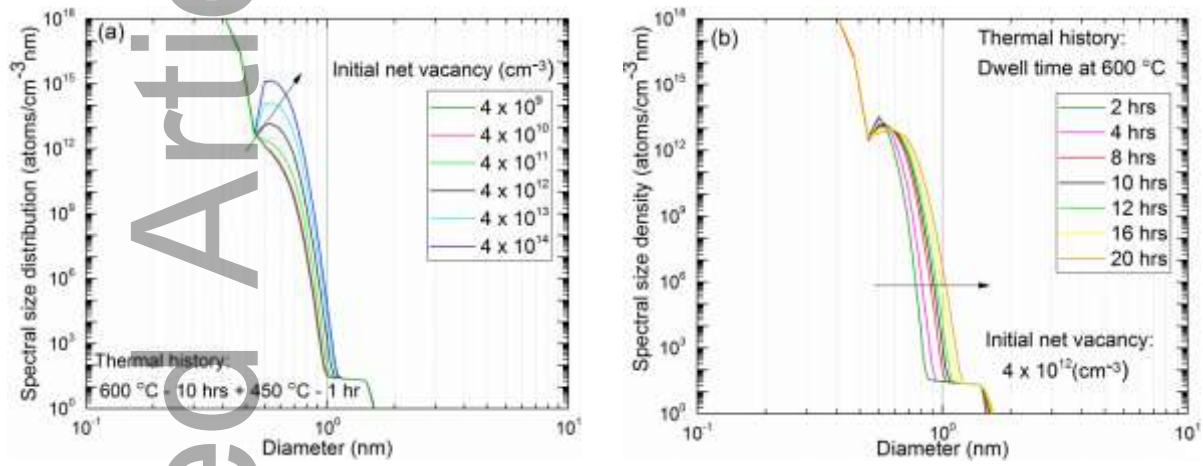


**Figure 6:** Simulated spectral size distributions of OP in the as-grown state of samples used in this work under different (a) net vacancy conditions and (b) dwell time at 600 °C.

### 5.3 Simulations of the TD generation and annihilation steps in the as-grown samples

**Figure 7** demonstrates the evolution of the spectral size distribution and OP density with an increase in the duration of a TD generation step followed by TD annihilation. The TD annihilation step does not show any significant influence on the spectral size distribution and OP density (not shown here). As expected, the average size of OPs increased monotonically with the TD generation duration, as shown in **Figure 7 (a)**. The 24 hrs TD generation treated sample has the largest concentration of OP with a maximum size greater than 6 nm in diameter. Such OPs are significantly larger than in the as-grown sample. Note the size of such precipitates ( $\sim 6 \text{ nm}$ ) still remains smaller than the detection limit of LST ( $> 15 - 20$

nm). It would thus be challenging to measure such trends experimentally. Further, our simulations suggest that ring-like defects in the sample treated for 24 hrs are primarily due to the size variation of OPs but not due to the overall density of OPs as both 24 hrs and 4 hrs TD generation treated samples have similar OP densities, as shown in **Figure 7 (b)**. Note previously, OPs formed at low-temperatures are demonstrated to exist in rod-like structure [19], [49]. Therefore, the assumption of spherical precipitate geometry in this work might underestimate the nucleation rates of OPs. Nevertheless, our simulations provide a qualitative demonstration that oxygen precipitation can occur at low-temperatures.

Furthermore, we investigate possible sources of striations due to these ring-like defects. We hypothesize that the ring-like features could originate during ingot growth, where microscopic growth rate fluctuations can induce inhomogeneous incorporation of intrinsic point defects along the radial direction [50], [51]. These inhomogeneities lead to non-uniform incorporation of point defects, which trigger local variations in the oxygen precipitation rate during the subsequent heat treatments [52]. As a result, after extended heat-treatment local variations in the size of OPs result in the inhomogeneous recombination activity distributions which induce ring-like defects in the sample. This hypothesis was tested in this work, with small-scale (1%) variations in the initial net vacancy concentration, representing inhomogeneity in the radial direction. This small variation in initial net vacancy concentration influences the spectral distribution of OPs, but has no significant impact on the maximum size, as shown in **Figure 7 (c)**. Therefore, the difference in the spectral size of OPs could induce local variation in recombination activity in the samples.

The simulated oxygen precipitation behavior and the net loss of  $[O_i]$  observed from the FTIR measurements strongly support the direct implication of OP in the formation of ring-like defects in our samples annealed at 450 °C. Note that a detailed quantification in potential



variation in oxygen precipitation should also consider the possible inhomogeneous distribution of  $[O_i]$  and net vacancy concentrations occurring during the process.

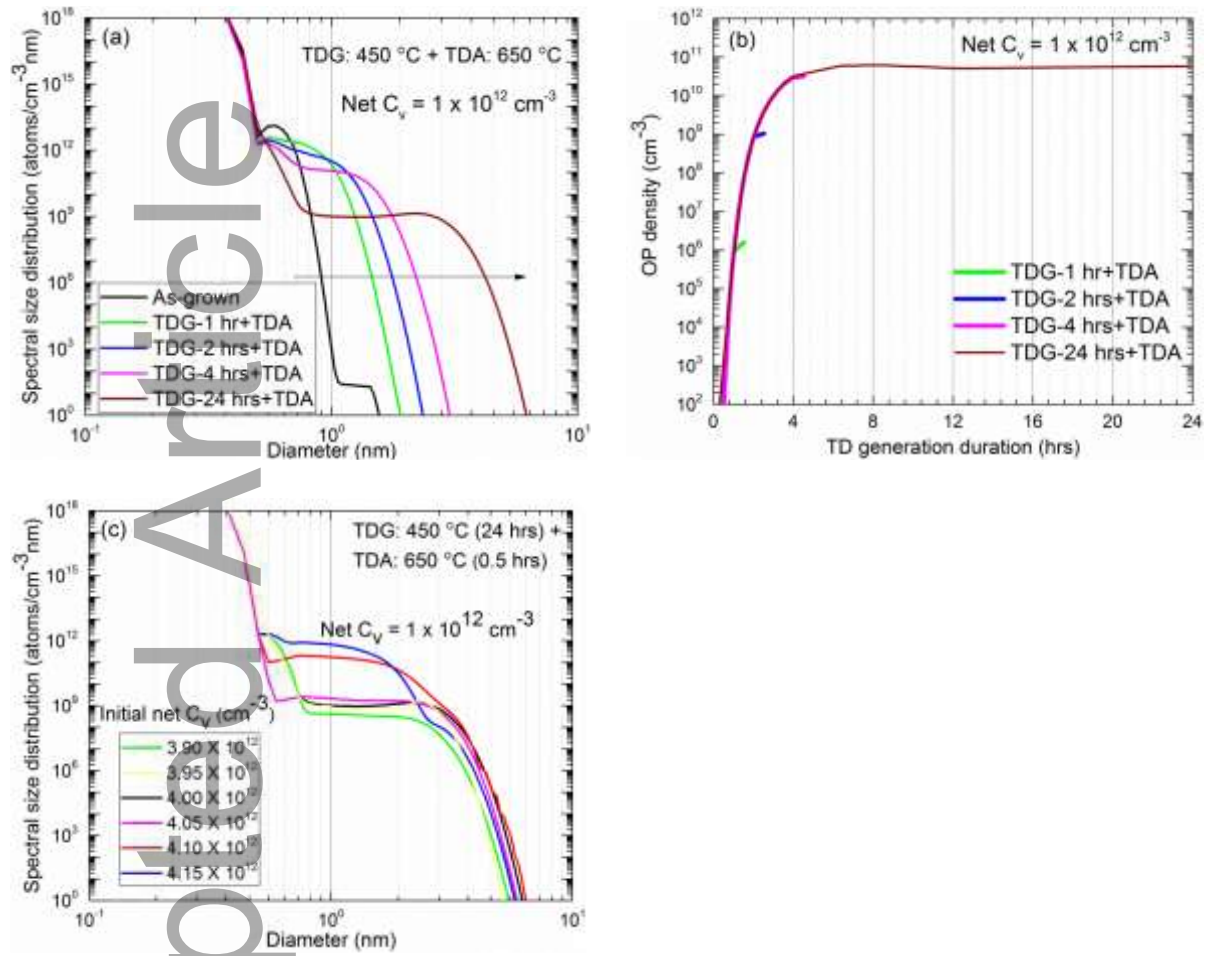


**Figure 7:** Simulated (a) spectral size distributions of OP and (b) OP densities in samples after TD generation steps followed by TD annihilation. (c) Comparison of spectral size distributions in 24 hrs TD generated + TD annihilated samples with the variations on the initial net vacancy concentration.

#### 5.4 Simulations of the TD generation and annihilation steps in the TR-treated samples

Further, we have simulated the possible impact of TR on the subsequent TD generation treatments, as shown in **Figure 8**. **Figure 8 (a)** compares the spectral size distribution of OP in the as-grown and TR-treated samples. As expected, the TR-treated sample shows a smaller

and narrower OP distribution, illustrating the dissolution of grown-in OP during TR. We compare the subsequent TD generation treatment of 24 hrs for the as-grown and TR-treated samples, as shown in **Figure 8 (b) and (c)**. The spectral size distribution of the TR-treated sample is smaller in comparison to the as-grown sample. More interestingly, the simulated precipitate density of OP is lower by an order of magnitude in the TR-treated samples. Therefore, the TR-treated samples have a lower net recombination-active defect concentration owing to both a small average size [53], [54], and low density of OP [55]–[57]. Hence, the onset of ring-like defects is delayed in the TR-treated sample, as shown in **Figure 5**.

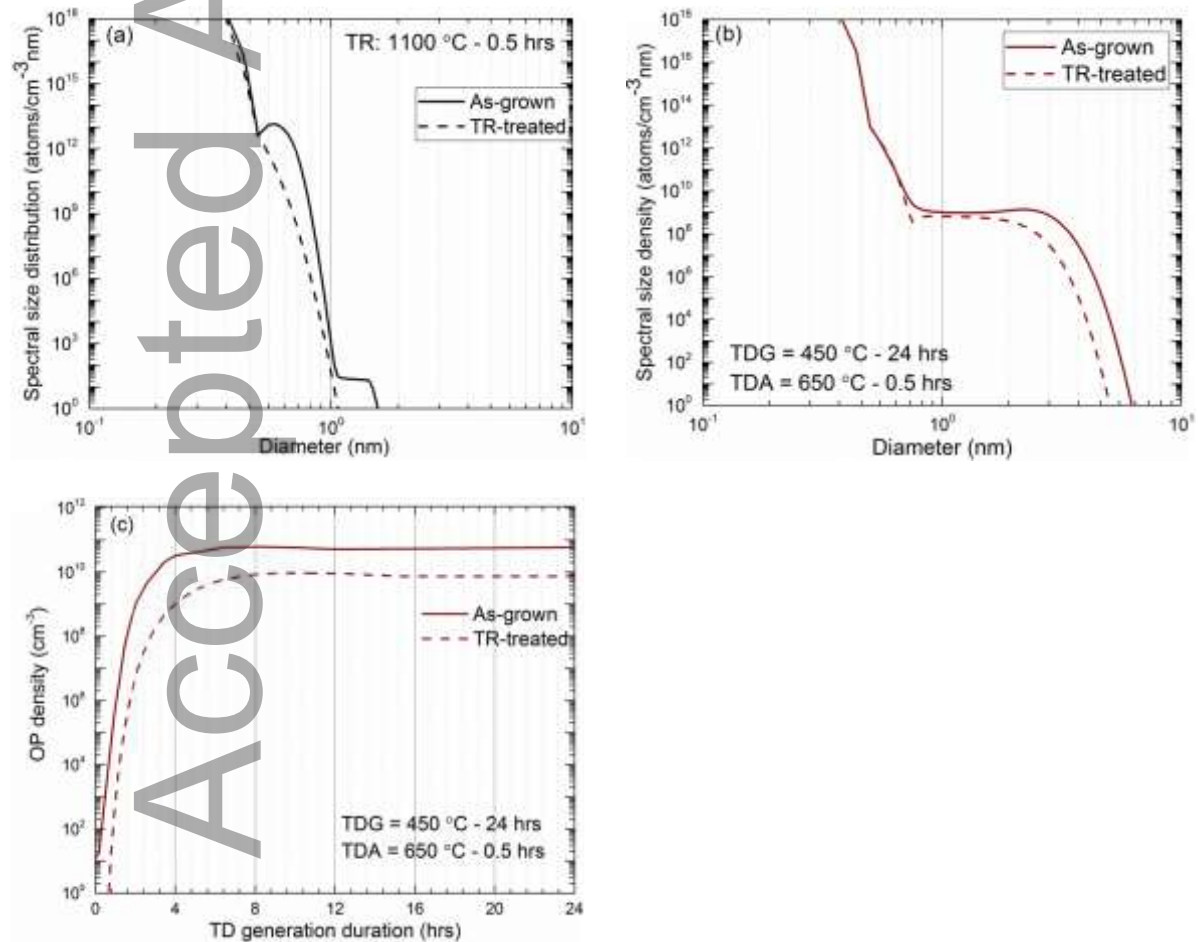


**Figure 8:** Comparison of simulated spectral size distributions of OP (a) in the as-grown and TR-treated state and (b) after subsequent 24 hrs TD generation followed by TD annihilation

step. (c) Comparison of simulated OP density after 24 hrs TD generation followed by subsequent TD annihilation step in the as-grown and TR-treated samples.

## 6.0 Discussion of defect formation

The experimental and simulation results of this work corroborate the formation of persistent recombination-active ring-like defects during 450 °C annealing of *n*-type Cz-Si wafers. The basic defect formation mechanism in this work can be qualitatively described by the schematic diagram shown in **Figure 9**. Samples are shown in two different initial states, namely as-grown and TR-treated. Then, the samples are subjected to low-temperature anneals. In general, as-grown samples are likely to have some grown-in TDs and OP nuclei. Therefore, a 450 °C heat-treatment of as-grown samples can generate TDs via two processes: (a) growth of grown-in TD nuclei, and (b) formation of new TD nuclei by the clustering of interstitial oxygen or oxygen dimers. During the initial stage of subsequent low-temperature anneal, TDs are predominately generated from the grown-in nuclei and later from the new nuclei formed during heat treatment. During the TD formation process, the agglomeration of  $O_i$  leads to the formation of a range of TD species. In one of the agglomeration processes, oxygen dimers agglomerate with interstitial oxygen and form an oxygen trimer ( $O_{3i}$ ) ( $O_i + O_{2i} \rightarrow O_{3i}$ ). The oxygen trimers are thought to be electrically-inactive TD clusters but act as heterogeneous nuclei for OPs [30], [58]. Therefore, in the course of the low-temperature annealing, some of the TD clusters continually act as the early stage of pre-cursors for OPs, which after extended annealing transform into OPs. The coexistence of electrically-active TDs and electrically-inactive OPs has been proposed by Wada and Inoue [40] which described the possible mechanism on the transformation of TDs into OP nuclei during the course of heat treatment.

In addition, during low-temperature heat treatments, some of the grown-in OP nuclei further grow and become recombination-active OPs. As a result, after sufficiently long TD generation anneals the size and density of OPs increase, enhancing the net recombination activity of the samples. These OPs are stable and can survive TD annihilation, which contribute to the bulk degradation by forming ring-like defects.

In the case of the TR-treated samples, all of the grown-in TDs and most of the grown-in OP nuclei are dissolved. However, during the initial stage of subsequent TD generation treatment, fewer TDs are formed, nevertheless, after a sufficiently long duration, TDs formation saturate. In the meantime, some of TDs transform into OP nuclei and later into the recombination-active OPs. Therefore, TR-treated samples have fewer recombination-active OPs than in the as-grown sample until certain anneal duration, but after a sufficiently long duration, similar OPs are expected.

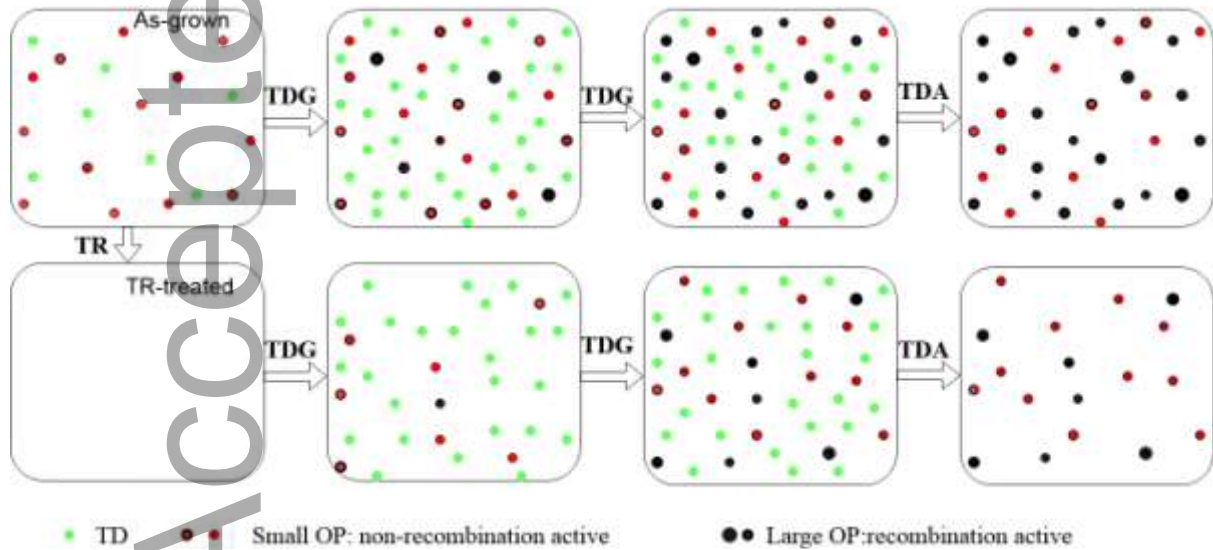


**Figure 9:** Schematic illustration of TD and OP evolution in as-grown and TR-treated samples after subjecting them to a 450 °C TD generation anneals and 600 °C TD annihilation anneal. Note that the two TD generation steps represent an increasing TD generation anneal duration.

## 7.0 Conclusions

In this work, we demonstrate the formation of persistent recombination-active ring-like defects during TD formation at 450 °C and investigate their origin. As expected, we observed a loss in the interstitial oxygen concentration during TD formation. However, unlike the resistivity, the loss in interstitial oxygen concentration does not recover completely after TD annihilation. Furthermore, in the samples used in this work, ring-like defects appear after 24 hrs of TD-generation anneal which do not disappear after TD annihilation. We utilize an oxygen precipitation model developed by Trzynadlowski [42], [43] to simulate the oxygen precipitation behavior at 450 °C. We assume an enhanced effective diffusivity of oxygen at 450 °C due to the presence of oxygen dimers. The resulting simulations support our findings that oxygen precipitation can occur and induce ring-like defects. Further, we find that pre-annealing can delay the onset of ring-like defects due to the dissolution of grown-in TD nuclei. Therefore, through the change in resistivity, net losses in interstitial oxygen concentration, ring-like defects in PL images, and simulations, we demonstrate the simultaneous formation of TDs and OPs in *n*-type Cz-Si wafers annealed at 450 °C. This result is critical to understand recombination-active defect formation during Cz-Si ingot growth. More importantly, this work further accentuates the vital role of optimized growth conditions of Cz-Si ingot with a short low-temperature dwell-time to suppress recombination-active defect generation.

## **Acknowledgment**

This work has been supported by the Australian Renewable Energy Agency (ARENA) through project RND017 and the Australian Centre for Advanced Photovoltaics (ACAP).

## **Conflict of Interest**

The authors declare no conflict of interest.

## **References**

- [1] J. Haunschild, I. E. Reis, J. Geilker, and S. Rein, *Phys. status solidi - Rapid Res. Lett.*, vol. 5, no. 5–6, pp. 199–201, Jun. 2011.
- [2] B. Martel, J. Veirman, M. Tomassini, M. Cascant, J. Le Perchec, R. Cabal, A. Danel, N. Enjalbert, C. Picoulet, and X. Brun, 2015.
- [3] R. Basnet, F. E. Rougieux, C. Sun, S. P. Phang, C. Samundsett, R. Einhaus, J. Degoulange, and D. Macdonald, *IEEE J. Photovoltaics*, vol. 8, no. 4, pp. 990–996, Jul. 2018.
- [4] M. Porrini, P. Collareta, G. Borionetti, D. Gambaro, and I. Fini, *Mater. Sci. Eng. B*, vol. 73, no. 1–3, pp. 139–144, Apr. 2000.
- [5] Y. Hu, H. Schøn, Ø. Nielsen, E. Johannes Øvrelid, and L. Arnberg, *J. Appl. Phys.*, vol. 111, no. 5, p. 053101, Mar. 2012.
- [6] E. Olsen, M. I. Helander, T. Mehl, and I. Burud, *Phys. status solidi*, vol. 217, no. 6, p. 1900884, Mar. 2020.
- [7] R. Basnet, C. Sun, H. Wu, H. T. Nguyen, F. E. Rougieux, and D. Macdonald, *J. Appl. Phys.*, vol. 124, no. 24, p. 243101, Dec. 2018.
- [8] A. Le Donne, S. Binetti, V. Folegatti, and G. Coletti, *Appl. Phys. Lett.*, vol. 109, no. 3, p. 033907, Jul. 2016.
- [9] H. Angelskår, R. Søndena, M. S. Wiig, and E. S. Marstein, *Energy Procedia*, vol. 27, pp. 160–166, 2012.
- [10] W. Götz, G. Pensl, and W. Zulehner, *Phys. Rev. B*, vol. 46, no. 7, pp. 4312–4315, Aug. 1992.
- [11] T. Hallberg and J. L. Lindström, *Appl. Phys. Lett.*, vol. 68, no. 24, pp. 3458–3460, Jun.

- 1996.
- [12] D. Wruck and P. Gaworzewski, *Phys. Status Solidi*, vol. 56, no. 2, pp. 557–564, Dec. 1979.
- [13] C. S. Fuller and R. A. Logan, *J. Appl. Phys.*, vol. 28, no. 12, pp. 1427–1436, Dec. 1957.
- [14] W. Kaiser, H. L. Frisch, and H. Reiss, *Phys. Rev.*, vol. 112, no. 5, pp. 1546–1554, Dec. 1958.
- [15] N. I. Puzanov and A. M. Eidenzon, *Semicond. Sci. Technol.*, vol. 12, no. 8, pp. 991–997, Aug. 1997.
- [16] R. Basnet, S. P. Phang, C. Sun, F. E. Rougieux, and D. Macdonald, *J. Appl. Phys.*, vol. 127, no. 15, p. 153101, Apr. 2020.
- [17] R. Basnet, S. P. Phang, C. Samundsett, D. Yan, W. Liang, C. Sun, S. Armand, R. Einhaus, J. Degoulange, and D. Macdonald, *Sol. RRL*, vol. 3, no. 11, p. 1900297, Nov. 2019.
- [18] J. C. Mikkelsen, *MRS Proc.*, vol. 59, p. 19, Feb. 1985.
- [19] K. Tempelhoff, F. Spiegelberg, R. Gleichmann, and D. Wruck, *Phys. Status Solidi*, vol. 56, no. 1, pp. 213–223, Nov. 1979.
- [20] T. Hallberg and J. L. Lindström, *J. Appl. Phys.*, vol. 79, no. 10, pp. 7570–7581, May 1996.
- [21] B. Sopori, P. Basnyat, S. Devayajanam, T. Tan, A. Upadhyaya, K. Tate, A. Rohatgi, and H. Xu, *IEEE J. Photovoltaics*, vol. 7, no. 1, pp. 97–103, Jan. 2017.

- [22] G. Pensl, M. Schulz, K. Holzlein, W. Bergholz, and J. L. Hutchison, *Appl. Phys. A Solids Surfaces*, vol. 48, no. 1, pp. 49–57, Jan. 1989.
- [23] R. A. Sinton and A. Cuevas, *Appl. Phys. Lett.*, vol. 69, no. 17, pp. 2510–2512, 1996.
- [24] T. Trupke, R. Bardos, M. Schubert, and W. Warta, *Appl. Phys. Lett.*, vol. 89, no. 4, pp. 044107–044107, 2006.
- [25] M. Claybourn and R. C. Newman, *Appl. Phys. Lett.*, vol. 52, no. 25, pp. 2139–2141, Jun. 1988.
- [26] M. Bruzzi, D. Menichelli, M. Scaringella, J. Härkönen, E. Tuovinen, and Z. Li, *J. Appl. Phys.*, vol. 99, no. 9, p. 093706, May 2006.
- [27] K. Wada, *Phys. Rev. B*, vol. 30, no. 10, pp. 5884–5895, Nov. 1984.
- [28] W. Wijaranakula, *Appl. Phys. Lett.*, vol. 59, no. 13, pp. 1608–1610, Sep. 1991.
- [29] B. -Y. Mao, J. Lagowski, and H. C. Gatos, *J. Appl. Phys.*, vol. 56, no. 10, pp. 2729–2733, Nov. 1984.
- [30] K. Torigoe and T. Ono, *AIP Adv.*, vol. 10, no. 4, p. 045019, Apr. 2020.
- [31] G. Gaspar, G. Coletti, M. Juel, S. Würzner, R. Søndena, M. Di Sabatino, L. Arnberg, and E. J. Øvrelid, *Sol. Energy Mater. Sol. Cells*, vol. 153, pp. 31–43, Aug. 2016.
- [32] R. J. Falster, M. Cornara, D. Gambaro, M. Olmo, and M. Pagani, *Solid State Phenom.*, vol. 57–58, pp. 123–128, Jul. 1997.
- [33] T. Tachibana, K. Nakamura, A. Ogura, Y. Ohshita, T. Shimoda, I. Masada, and E. Nishijima, *AIP Adv.*, vol. 7, no. 4, p. 045111, Apr. 2017.
- [34] R. Falster and V. . Voronkov, *Mater. Sci. Eng. B*, vol. 73, no. 1–3, pp. 87–94, Apr.

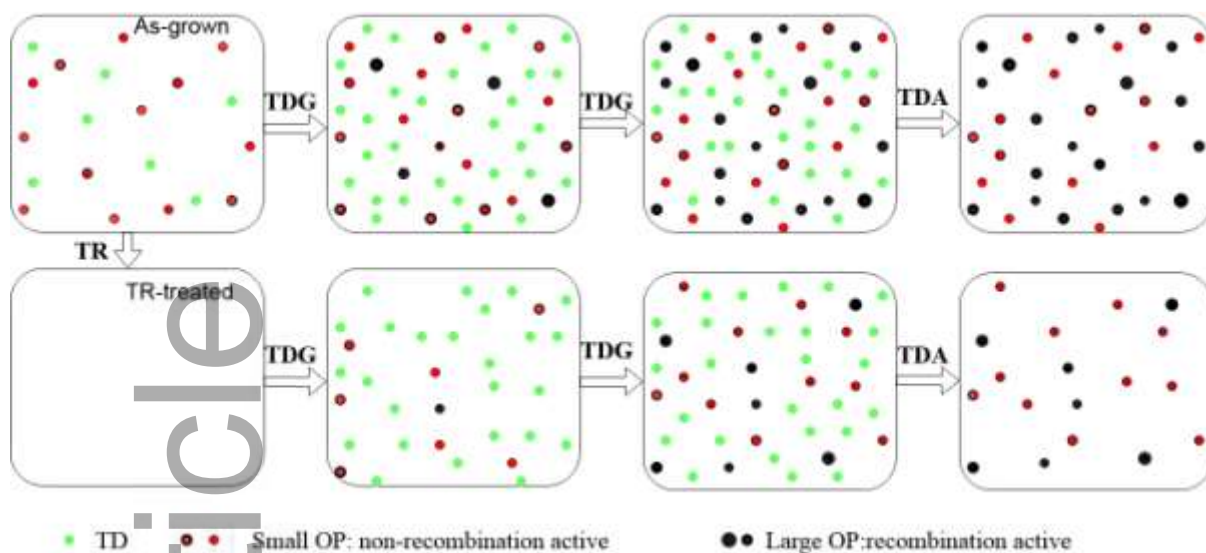


2000.

- [35] D. Åberg, B. G. Svensson, T. Hallberg, and J. L. Lindström, *Phys. Rev. B*, vol. 58, no. 19, pp. 12944–12951, Nov. 1998.
- [36] G. Kissinger, J. Dabrowski, V. D. Akhmetov, A. Sattler, D. Kot, and W. von Ammon, *Solid State Phenom.*, vol. 156–158, pp. 211–216, Oct. 2009.
- [37] S. A. McQuaid, B. K. Johnson, D. Gambaro, R. Falster, M. J. Ashwin, and J. H. Tucker, *J. Appl. Phys.*, vol. 86, no. 4, pp. 1878–1887, Aug. 1999.
- [38] S. -Ton. Lee, P. Fellingner, and S. Chen, *J. Appl. Phys.*, vol. 63, no. 6, pp. 1924–1927, Mar. 1988.
- [39] H. Takeno, Y. Hayamizu, and K. Miki, *J. Appl. Phys.*, vol. 84, no. 6, pp. 3113–3117, Sep. 1998.
- [40] K. Wada and N. Inoue, in *Semiconductor silicon*, 1986, p. 778.
- [41] K. F. Kelton, *Philos. Trans. R. Soc. London. Ser. A Math. Phys. Eng. Sci.*, vol. 361, no. 1804, pp. 429–446, Mar. 2003.
- [42] B. Trzynadlowski, University of Washington, 2013.
- [43] B. C. Trzynadlowski and S. T. Dunham, *J. Appl. Phys.*, vol. 114, no. 24, p. 243508, Dec. 2013.
- [44] S. T. Dunham, *J. Electrochem. Soc.*, vol. 142, no. 8, pp. 2823–2828, Aug. 1995.
- [45] G. Kissinger, in *Lecture Notes in Physics*, Lecture no., vol. 916, Springer, 2015, pp. 273–341.
- [46] J. Veirman, E. Letty, W. Favre, M. Albaric, D. Pelletier, and M. Lemiti, *Phys. status*

*solidi*, vol. 216, no. 17, p. 1900317, Sep. 2019.

- [47] A. Virzi and M. Porrini, *Mater. Sci. Eng. B*, vol. 17, no. 1–3, pp. 196–201, Feb. 1993.
- [48] E. Letty, University of Lyon, 2017.
- [49] W. Bergholz, J. L. Hutchison, and P. Pirouz, *J. Microsc.*, vol. 141, no. 2, pp. 143–154, Feb. 1986.
- [50] T. Abe, *J. Cryst. Growth*, vol. 24–25, pp. 463–467, Oct. 1974.
- [51] J. A. Burton, R. C. Prim, and W. P. Slichter, *J. Chem. Phys.*, vol. 21, no. 11, pp. 1987–1991, Nov. 1953.
- [52] A. J. R. de Kock, *Appl. Phys. Lett.*, vol. 16, no. 3, pp. 100–102, Feb. 1970.
- [53] J. M. Hwang and D. K. Schroder, *J. Appl. Phys.*, vol. 59, no. 7, pp. 2476–2487, Apr. 1986.
- [54] J. D. Murphy, M. Al-Amin, K. Bothe, M. Olmo, V. V. Voronkov, and R. J. Falster, *J. Appl. Phys.*, vol. 118, no. 21, p. 215706, Dec. 2015.
- [55] M. Miyagi, K. Wada, J. Osaka, and N. Inoue, *Appl. Phys. Lett.*, vol. 40, no. 8, pp. 719–721, Apr. 1982.
- [56] J. D. Murphy, K. Bothe, M. Olmo, V. V. Voronkov, and R. J. Falster, *J. Appl. Phys.*, vol. 110, no. 5, p. 053713, Sep. 2011.
- [57] J. D. Murphy, K. Bothe, R. Krain, V. V. Voronkov, and R. J. Falster, *J. Appl. Phys.*, vol. 111, no. 11, p. 113709, Jun. 2012.
- [58] L. I. Murin, B. G. Svensson, J. L. Lindström, V. P. Markevich, and C. A. Londos, *Phys. B Condens. Matter*, vol. 404, no. 23–24, pp. 4568–4571, Dec. 2009.



The simultaneous formation of ring-like defects and thermal donors at a 450 °C anneal is experimentally elucidated. The results are then corroborated by adopting an enhanced effective diffusivity of oxygen at 450 °C together with an oxygen precipitation model to simulate oxygen precipitation kinetics during the 450 °C annealing steps.